A Modified Double Gyre with Ground Truth Hyperbolic Trajectories for Flow Visualization

S. Wolligandt, T. Wilde, C. Rössl, H. Theisel

University of Magdeburg

Abstract
The model of a DOUBLE GYRE *flow by Shadden et al. [SLM05] is a standard benchmark data set for the computation of hyperbolic Lagrangian Coherent Structures (LCS) in flow data. While structurally extremely simple, it generates hyperbolic LCS of arbitrary complexity. Unfortunately, the* DOUBLE GYRE *does not come with a well-defined ground truth: the location of hyperbolic LCS boundaries can only be approximated by numerical methods that usually involve the gradient of the flow map. We present a new benchmark data set that is a small but carefully designed modification of the* DOUBLE GYRE*, which comes with ground truth closed-form hyperbolic trajectories. This allows for computing hyperbolic LCS boundaries by a simple particle integration without the consideration of the flow map gradient. We use these hyperbolic LCS as a ground truth solution for testing an existing numerical approach for extracting hyperbolic trajectories. In addition, we are able to construct hyperbolic LCS curves that are significantly longer than in existing numerical methods.*

1. Introduction

The analysis of hyperbolic Lagrangian Coherent Structures (LCS) is a standard problem in several fields like dynamical systems, physics and flow visualization. It has been subject of an intensive research over the last decade. Most modern hyperbolic LCS concepts consider the gradient of the flow map of a velocity field. This gradient field is known to be challenging: even if the velocity field is numerically well-behaved – i.e., velocity and its gradient are smooth and bounded – the gradient of the flow map can increase exponentially with increasing integration time, which makes an extremely careful sampling of the flow map necessary.

Once new techniques for hyperbolic LCS extraction and analysis are developed, they need to be evaluated for some test data to verify correctness and accuracy and desired properties empirically before they can be applied to real world flow data. Such test data should have the following properties:

- They should have a simple form, ideally as a closed formula.
- They should generate LCS of complexity and ffticulty comparable to what is expected in the real data.
- The ground truth – i.e., the correct locations of the LCS – should be either known or be trivially computable with high accuracy, i.e., without consideration of the flow map gradient.

A double gyre is a flow pattern that frequently occurs in geophysical flows [HS19a, AU01, SMW99]. In 2005, Shadden et al. [SLM05] introduce a simple model of a double gyre that became a success story among LCS test data sets. It is just a simple closed

formula of a 2D time-dependent velocity field that produces LCS of arbitrary complexity. With increasing integration time, length and density of hyperbolic LCS increase exponentially, which makes the DOUBLE GYRE a perfect tool for testing hyperbolic LCS extraction methods. In the remainder of this paper, DOUBLE GYRE refers to the particular data set in [SLM05] rather than to the general flow pattern.

After its introduction by Shadden et al. [SLM05], the DOUBLE GYRE became omnipresent in the LCS and flow visualization literature. (The original paper has been cited more than 1 000 times, a significant subset of them, we estimate several hundreds, use the DOUBLE GYRE data set.) In recent years there is hardly any paper on hyperbolic LCS extraction that does not test its methods on the DOUBLE GYRE. There are even papers [BK17] that use the DOUBLE GYRE without mentioning its original source [SLM05]. The success of the DOUBLE GYRE as benchmark data comes from the combination of an extremely simple closed-form description and an arbitrary complex output in terms of hyperbolic LCS.

Despite its success, the DOUBLE GYRE comes with a significant shortcoming: Given a certain integration time, the exact positions of the LCS are unknown. In fact, they can only be computed numerically by analyzing the flow map gradient, making them prone to numerical errors.

The key to computing 2D hyperbolic LCS are *hyperbolic trajectories* and their local stable and unstable manifolds [Hal00]. In fact, "finite-time Lyapunov exponents and finite strain maps approximate the set of all global stable and unstable manifolds that

could be more accurately reproduced numerically if one knew the exact location of some organizing orbits with strong or, uniform, hyperbolicity." [Hal00]. Knowing the hyperbolic trajectories in a velocity field reduces the hyperbolic LCS extraction to a simple and stable particle integration without consideration of the flow map gradient. This way, hyperbolic LCS and hyperbolic trajectories can be treated synonymously: once we have the perfect hyperbolic LCS, hyperbolic trajectories are part of them. Conversely, if we have hyperbolic trajectories, the whole hyperbolic LCS can be obtained almost for free, i.e. by numerical integration that relies only on the location and not in the derivative of the flow map.

For the DOUBLE GYRE, neither the location of hyperbolic LCS nor of the hyperbolic trajectories are known in a closed form. An analysis of the DOUBLE GYRE shows that the numerically extracted hyperbolic trajectory looks very similar to a sine curve. However, there is no closed form description of the hyperbolic trajectories of the DOUBLE GYRE, and hence numerical methods are necessary to approximate them. Our goal is to make a small modification of the DOUBLE GYRE that makes its hyperbolic trajectory a perfect sine curve that can be described as a closed-from solution. It turns out that such representation can be found and that this can be done with a reparametrization of the time domain.

In this paper we introduce a new benchmark data set that is a small modification of the DOUBLE GYRE with the following properties:

- It should be close to the DOUBLE GYRE and in particular should have LCS of similar complexity.
- Contrary to the DOUBLE GYRE, the hyperbolic trajectories are known in a closed form. This allows for computing hyperbolic LCS by a stable and well-behaved particle integration, i.e., without any consideration of the flow map gradient.

We utilize our *Modified Double Gyre* in an evaluation of existing techniques for the extraction of hyperbolic trajectories, and for an evaluation of the quality of existing ridge line extractors in 2D Finite-Time Lyapunov Exponent (FTLE) scalar fields.

Notation. We denote the DOUBLE GYRE as $\mathbf{v}(\mathbf{x},t) = \mathbf{v}(x,y,t)$ and the corresponding flow map as $\phi_t^\tau(\mathbf{x})$, i.e., $\frac{\partial}{\partial \tau}\phi_t^\tau(\mathbf{x}) = \mathbf{v}(\phi_t^\tau(\mathbf{x}), t+\tau)$. We also consider the spatial gradient $\nabla\phi = \frac{d\phi}{d\mathbf{x}}$ of the flow map. The new *Modified Double Gyre* is named $\bar{\mathbf{v}}(\mathbf{x},t)$ and comes with its flow map $\bar{\phi}_t^\tau(\mathbf{x})$ and its flow map gradient $\nabla\bar{\phi}$. $\mathbf{I}$ denotes the unit matrix.

2. The Modified Double Gyre data set in a nutshell

Given the DOUBLE GYRE $\mathbf{v}(\mathbf{x},t)$ [SLM05, Sha05] as in (7)−(11), we propose a *Modified Double Gyre*

$$\bar{\mathbf{v}}(\mathbf{x},t) = \mathbf{v}(\mathbf{x},t+p)$$

with

$$p = p(t) = \frac{\arcsin(q)}{\omega} - t$$

$$q = q(t) = \frac{-\pi c \sin(r) + \arcsin\left(\frac{c\,\omega\cos(r)}{A\pi}\right)}{\pi\varepsilon\,(c^2\sin(r)^2 - 1)}$$

$$r = r(t) = \omega t + d.$$

This data set has the sine curve

$$\mathbf{g}(t) = \begin{pmatrix} c\sin(r)+1 \\ 0 \end{pmatrix}$$

as ground truth hyperbolic trajectory. For the particular parameter choice (15) of the DOUBLE GYRE, we set

$$c = -0.2040811331, \quad d = 9.964223388 .$$

3. Related Work

LCS are coherent trajectory patterns in flows that preserve certain properties over a (finite or infinite) integration time [Hal15]. Different types of LCS are known [HFB*17]: elliptic (vortex type), hyperbolic (attracting or repelling), and parabolic (jet core type) structures. Since the Double Gyre resembles hyperbolic LCS, we focus on hyperbolic LCS here.

Flow Benchmark Datasets. Several benchmark data sets are being used in the literature. Some examples for analytical two-dimensional data sets are the DOUBLE GYREby Shadden [SLM05], multiple variations of the forced Duffing equation [HS11] [RSPB11] [FH13] and a Bickley jet [RSPB11] [OHH15]. In his papers Haller has also used some simpler, unnamed flows (e.g. [Hal02a] [Hal11]). Analytical examples for three-dimensional flows include the ABC-Flow [Mof88], a Rayleigh-Benard-Convection [LSM06] or a tornado flow [Cra03]. Moreover there are several simulated data sets like cylinder flow simulations [GGT17] [KC93], backward facing step simulations [GSM*14] [BAC93] or delta wing simulations [PNNS88] [PNNS86]. However, we are not aware of a benchmark data set that is as widespread as the DOUBLE GYRE.

Hyperbolic trajectories. Hyperbolic trajectories are the key to understanding hyperbolic LCS. Haller [Hal00] defines hyperbolic trajectories as trajectories (path lines) with a maximal hyperbolicity time d_T, i.e., the trajectory spends a maximal time within an area where the determinant of the Jacobian of $\mathbf{v}$ is negative. In fact, [Hal00] gives conditions for a trajectory $\mathbf{x}(t)$ to be a HT:

$$\det\nabla\mathbf{v}(\mathbf{x}(t),t) < 0 \text{for all} t \in [t_0, t_0+T] \tag{1}$$

$$\sqrt{2}\beta\left(\frac{1}{\lambda_{1_{min}}} + \frac{1}{\lambda_{2_{min}}}\right) < \alpha \tag{2}$$

with

$$\mathbf{J}(t) = \nabla\mathbf{v}(\mathbf{x}(t),t) = \mathbf{M}(t)\begin{pmatrix} -\lambda_1(t) & 0 \\ 0 & \lambda_2(t) \end{pmatrix}(\mathbf{M}(t))^T, \tag{3}$$

i.e., the eigenvalues of $\mathbf{J}$ are $-\lambda_1 < 0 < \lambda_2$ and the columns of $\mathbf{M}$ contain the corresponding normalized eigenvectors of $\mathbf{J}$, and

$$\lambda_{k_{min}} = \min_{[t_0,t_0+T]} \lambda_k(t) \quad, \quad k = 1,2 \tag{4}$$

$$\alpha = \min_{[t_0,t_0+T]} \|\det\mathbf{M}\| \tag{5}$$

$$\beta = \max_{[t_0,t_0+T]} \left\|\frac{d\mathbf{M}}{dt}\right\|. \tag{6}$$

Based on this, a number of approaches for the numerical extraction of hyperbolic trajectories have been proposed. [Hal00] considers the local maxima of the hyperbolicity time in both forward

and backward direction. [ÜSE13] finds hyperbolic trajectories by intersecting the ridges of forward and backward FTLE. In addition to these integration-based methods, local methods to get hyperbolic trajectories have been proposed. Haller [HP98] shows that under certain conditions the location of critical saddle points of **v** can represent hyperbolic trajectories. Machado et al. [MBES16] relate hyperbolic trajectories to bifurcation lines [PC87], [MSE13] and present a two-step approach for the extraction: first, the location of vanishing acceleration **a** or jerk **b** of the vector field **v** are found as initial values of an optimization which moves in a second step these initial lines towards a path line of **v**. This way a localized approach (i.e., without computing the flow map of **v**) to get hyperbolic trajectories is obtained.

Once the hyperbolic trajectories are found, there are several well-established approaches to compute the corresponding stable and unstable manifolds [YKY91, MSWI03]. [MBES16, ÜSE13, SW10] compute generalized streak lines starting in the neighborhood of the hyperbolic trajectories.

Finite-Time Lyapunov Exponents (FTLE): FTLE is one of the most common approaches to define and extract hyperbolic LCS. Even though its pros and cons are well-studied and a number of alternative LCS concepts is available, FTLE is still among the most prominent approaches to extract hyperbolic LCS, in particular in Flow Visualization. The FTLE is a well known scalar measure, that describes the temporal "'stretch'" of particles released in a flow. Haller introduced the extraction of ridge structures in FTLE fields, which correspond to LCS in flow fields [HY00, Hal01, Hal02b]. Shadden et al. [SLM05] show that for increasing integration time ridges of FTLE fields converge approximately to material structures. A general introduction into LCS and their use for describing flow dynamics is given in [Hal15], whic explaines how LCS boundaries can be extracted via FTLE ridges. However it also states that there are several issues of FTLE in the context of LCS-extraction.

FTLE and its ridges have been used in various applications: Lekien et al. [LCM*05] and Coulliette et al. [CLP*07] use FTLE ridges to describe the pollution process of coastal environments in bay areas. Andrade-Canto et al. [ACSZ13] use backward FTLE to predict the behavior of Eddies in the Gulf of Mexico. Wilde et al. [WRT18] track FTLE ridges by increasing the resolution in regions where ridges evolve over integration time; they also extract the ridge geometries. A lot of research is dedicated to improving performance and accuracy of FTLE ridge computation [GGTH07, SP07, GLT*09, SP09, GOPT11, HSW11, PPF*11, SRP11].

Most of the approaches mentioned above restrict themselves to ridge curves in 2D flows. There are also few approaches that extract ridge surfaces in 3D flows for moderate integration times. Sadlo and Peikert [SP07] present FTLE ridge surfaces where care is taken on an adaptive grid generation. Schindler et al. [SPFT12] show both, standard height ridge extraction and C-ridge tracking to get 3D surfaces. [SFB*12] show C-ridge surfaces for an analysis of revolving doors. Üffinger et al. [ÜSE13] present streak surfaces as approximations to LCS. Depending on the accuracy of the seed structures (obtained by extremely high sampling), streak surfaces and FTLE ridges show strong agreement. [BT13] propose an adaptive smooth reconstruction of the flow map field from the

sample points based on Sibson's interpolation, which gives a more stable ridge extraction than on the original sampling. The results could be used as a qualitative ground truth, a quantitative solution is missing.

Periodic vector fields. Periodic vector fields are a special case for which the treatment of hyperbolic trajectories is significantly more simple: they correspond to the identities in the Poincare map with negative determinant of the Jacobian [HP98, RK94, Wig92]. In flow visualization, this has been exploited in [STW*06]. We mention this because the Double Gyre (as well as the new modified Double Gyre) are periodic; we will use this periodicity for our contribution.

Double Gyre data set. The DOUBLE GYRE data set was introduced by Shadden et al. [SLM05]. It mimics a Double Gyre pattern, which typically occurs in various geophysical flows. The core idea was to provide an analytic form of a time-varying vector field showing such behavior that stays within a rectangular domain. The paper provides the stream-function, the corresponding velocity field and studies material transport over extracted LCS. In the following we list some typical examples that use the DOUBLE GYRE as a benchmark to show both its importance and versatility. Germer et al. [GOPT11] study guaranteed material separation along LCS. Schindler et al. [SPFT12] evaluate new ridge concepts for LCS. [BT13] and [WRT18] evaluate adaptive refinement strategies for the flow map as well as extraction of ridge geometries. Machado et al. [MBES16] extract LCS via space time bifurcation lines. Günther et al. [GKT16] present a method that computes high quality FTLE ridges and ridge surfaces based on Monte-Carlo path tracing. Hummel et al. [HBJG16] analyze an error estimation for Lagrangian representations of flows. Hofmann et al. [HS19b] extract recirculation surfaces [WRT19] with the dependent vectors operator in 2D. [FS16] uses the Double Gyre to study mixing enhancement, while [FP09] considers almost-invariant manifolds with the help pf the Double Gyre.

The DOUBLE GYRE is given with a set of parameters that can be altered to influence the behavior of the flow. Although most works use the original parameters given by Shadden et al. , other versions exist: For instance, Sadlo et al. [SW10] extend the domain, to receive a flow field consisting of four rotating gyres. Wilde et al. [WRT19] provide a 3D version of the DOUBLE GYRE.

LCS ground truth. In order to evaluate the accuracy of techniques for extracting hyperbolic LCS the results have to be compared to a ground truth. Preferably the ground truth is given in a closed-form, to allow for an evaluation for any desired parameter at the highest possible accuracy. Unfortunately for realistic flow data sets no such closed forms exist. Kuhn et al. [KRWT12] provide artificial non-trivial vector fields with closed-form solutions for the corresponding FTLE fields. These could be used to (numerically) determine LCS. While they provide fields with ground truth FTLE ridges, these ridges are less complex as, e.g., the DOUBLE GYRE for longer integration times. [RG19] introduces a modification of the Double Gyre based on a domain deformation. Similar to [KRWT12], this approach cannot produce LCS of a similar complexity as the DOUBLE GYRE.

4. The Double Gyre Flow

The DOUBLE GYRE by Shadden et al. [SLM05] is defined by a 2D time-dependent stream function

$$\psi(\mathbf{x},t) = A\sin(\pi f(x,t))\sin(\pi y) \qquad (7)$$

with

$$f(x,t) \;= a(t)x^2 + b(t)x \qquad (8)$$

$$a(t) \quad\; = \varepsilon\sin(\omega t) \qquad (9)$$

$$b(t) \;= 1 - 2\varepsilon\sin(\omega t). \qquad (10)$$

Then the DOUBLE GYRE is the co-gradient of ψ:

$$\mathbf{v}(\mathbf{x},t) = \begin{pmatrix} 0 & -1 \\ 1 & 0 \end{pmatrix}\nabla\psi\,, \qquad (11)$$

which is usually considered within the spatial domain $[0,2]\times[0,1]$. Note that both $\mathbf{v}$ and $\nabla\mathbf{v}$ are bounded. In fact, for $\mathbf{x}\in[0,2]\times[0,1]$ we have $\|\mathbf{v}\| < 1$ and $\|\nabla\mathbf{v}\| < 4$ for the usual parameter settings (15). This means that we can expect a numerical integration of $\mathbf{v}$ to be stable, even for longer integration times. Since particles never leave the domain $[0,2]\times[0,1]$, we can also expect the computation of the flow map ϕ to be stable. Contrarily, the gradient of the flow map $\nabla\phi$ experiences an exponential increase in magnitude with respect to the integration time. This fact makes the exact numerical computation of $\nabla\phi$ challenging.

The DOUBLE GYRE comes with the time periodicity

$$\mathbf{v}(\mathbf{x},t) = \mathbf{v}(\mathbf{x},t + i\frac{2\pi}{\omega}) \qquad (12)$$

and the mirror time symmetries

$$\mathbf{v}(\mathbf{x},\frac{\pi}{2\omega} + i\frac{\pi}{\omega} - t) = \mathbf{v}(\mathbf{x},\frac{\pi}{2\omega} + i\frac{\pi}{\omega} + t) \qquad (13)$$

for any integer $i\in\mathbb{Z}$ where (13) can be rewritten as

$$\mathbf{v}(\mathbf{x},t) = \mathbf{v}(\mathbf{x},\frac{\pi(2i+1)}{\omega} - t)\,. \qquad (14)$$

Usually, the DOUBLE GYRE is considered with the parameters

$$\varepsilon = \frac{1}{4}\,,\ \omega = \frac{2\pi}{10}\,,\ A = \frac{1}{10} \qquad (15)$$

resulting in the periodic data set with the time period $t = 10$.

5. The Modified Double Gyre

Our goal is a small modification of the DOUBLE GYRE that makes a sine curve a hyperbolic trajectory. We consider the particular sine curve

$$\mathbf{g}(t) = \begin{pmatrix} g(t) \\ 0 \end{pmatrix} = \begin{pmatrix} c\sin(r) + 1 \\ 0 \end{pmatrix} \qquad (16)$$

with

$$r = r(t) = \omega t + d.$$

Note that $\mathbf{g}(t)$ has the same periodicity as $\mathbf{v}$, i.e., $\mathbf{g}(t) = \mathbf{g}(t + i\frac{2\pi}{\omega})$ for any integer $i\in\mathbb{Z}$. Also, $\mathbf{g}(t)$ comes with two parameters c and d, which will be discussed later on.

Our approach to modifying the DOUBLE GYRE is to apply a

"slight" reparametrization in time, i.e., we define the *Modified Double Gyre* as

$$\bar{\mathbf{v}}(\mathbf{x},t) = \mathbf{v}(\mathbf{x},t + p)\,, \qquad (17)$$

where $p = p(t)$ describes the reparametrization in time. The function p should have the following properties:

- p should be rather small: the smaller p, the more similar are $\mathbf{v}$ and $\bar{\mathbf{v}}$.
- p should have the same periodicity as $\mathbf{v}$: $p(t) = p(t + i\frac{2\pi}{\omega})$. This ensures that $\mathbf{v}$ and $\bar{\mathbf{v}}$ have the same time periodicity.
- p should ensure that $\mathbf{g}(t)$ is a hyperbolic trajectory of $\bar{\mathbf{v}}$.

Since by definition a hyperbolic trajectory is a path line of $\bar{\mathbf{v}}$, we need to solve

$$\frac{d\,\mathbf{g}(t)}{dt} = \bar{\mathbf{v}}(\mathbf{g}(t),t) = \mathbf{v}(\mathbf{g}(t),t + p) \qquad (18)$$

for the unknown function $p = p(t)$. Fortunately, (18) has a closed-form solution:

$$p = p(t) = \frac{\arcsin(q)}{\omega} - t \qquad (19)$$

with

$$q = q(t) = \frac{-\pi c\sin(r) + \arcsin\left(\frac{c\,\omega\cos(r)}{A\,\pi}\right)}{\pi\varepsilon(c^2\sin(r)^2 - 1)}. \qquad (20)$$

The proof that (19) and (20) are the solutions of (18) is in the appendix.

It remains to be shown that $\mathbf{g}(t)$ is indeed a hyperbolic trajectory of $\bar{\mathbf{v}}$. For this we consider the Jacobian matrix of $\bar{\mathbf{v}}$ along $\mathbf{g}(t)$:

$$\bar{\mathbf{J}}(t) = \nabla\bar{\mathbf{v}}(\mathbf{g}(t),t) \qquad (21)$$

for which it can be shown that it has the form

$$\bar{\mathbf{J}}(t) = \begin{pmatrix} h & 0 \\ 0 & -h \end{pmatrix} \qquad (22)$$

with

$$h = h(t) = 2\pi\sqrt{-c^2\omega^2\cos(r)^2 + A^2\pi^2}\left(\sin(r)c\,\varepsilon\,q + \frac{1}{2}\right). \qquad (23)$$

The proof that the Jacobian matrix (21) along $\mathbf{g}$ has indeed the form (22), (23) is in the appendix as well. If we assume

$$h(t) > 0 \qquad (24)$$

for all $t\in\mathbb{R}$, (22) gives (1) for arbitrary T. In other words, the hyperbolicity time of $\mathbf{g}(t)$ is infinity for both forward and backward integration, the trajectory never leaves a hyperbolic area. Furthermore, (22),(24) give for (4)–(6) by

$$\lambda_{1_{min}} = \lambda_{1_{min}} > 0\,,\ \mathbf{M} = \mathbf{I}\,,\ \alpha = 1\,,\ \beta = 0. \qquad (25)$$

This proves (2). With this the proof that $\mathbf{g}(t)$ is a hyperbolic trajectory of $\bar{\mathbf{v}}$ for arbitrary long integration times under the assumption (24) is done.

In order to finalize the proof (i.e. to show (24)), we switch to the particular parameter setting (15) in which the Double Gyre is usually considered. The function $p(t)$ needs some further consideration to become applicable. On the one hand, $p(t)$ contains
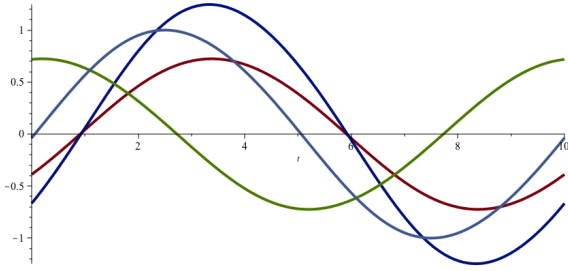
Figure 1: *The function $q(t)$ for different choices of c and d Blue: $c = 0.25, d = 0$; red: $c = 0.15, d = 0$; blue: $c = 0.15, d = 2$; light blue: $c = -0.2040811331, d = 9.964223388$. The light blue is the optimal function $q(t)$ obtained by solving (26). Note that c gives a (non-linear) scaling and d a domain translation. Also note that $q(t)$ is not a sine curve.*

arcsine functions for which we have to make sure that the arguments are within the interval $[-1, 1]$, and that – since arcsine is not injective: all $(-1)^i \arcsin(x) + i\pi$ have the same value for $i \in \mathbb{Z}$ – we pick the "correct" function value. Moreover, we have to find the best parameters c and d of the desired hyperbolic trajectory. To do so, we analyze the function $q(t)$. Figure 1 shows $q(t)$ for different parameters c and d. Note that even if $q(t)$ looks similar to a sine curve, it is *not*! (If it was a perfect sine curve, (19) would give that $p(t) = $ const, meaning that $\mathbf{g}(t)$ would be already a hyperbolic trajectory of $\mathbf{v}$.)

We want to chose c and d such that $q(t)$ comes as close as possible to a sine curve with periodicity 10. This means that $q(t)$ should have a local maximum of 1 at the location $t = \frac{5}{2}$. For this we need to solve the following system of equations

$$q\left(\frac{5}{2}\right) = 1 \; , \frac{dq}{dt}\left(\frac{5}{2}\right) = 0 \qquad (26)$$

for the unknowns c, d. Unfortunately, we are not aware of a closed-form solution of (26). However, we can solve (26) numerically (see the accompanying Maple sheet) resulting in the following approximate solutions:

$$c = -0.2040811331 \quad \text{and} \quad d = 9.964223388 \, . \qquad (27)$$

This gives the optimal function $q(t)$ that is shown as the light blue curve in figure 1. Note that it is close to but not exactly the function $\sin\frac{\pi t}{5}$. If it was, (19) would yield $p(t) = 0$. Figure 2 (left) shows a visual comparison of the optimal function q fulfilling (27) and the function $\sin\frac{\pi t}{5}$. The numerical solution of (27) may introduce a numerical error. This error does not infer the property of $\bar{\mathbf{v}}$ having the closed form hyperbolic trajectory, but it may affect the distance of $\mathbf{v}$ and $\bar{\mathbf{v}}$. However, a parameter study shows that the solutions are stable under perturbations of c, d. Figure 2(right) shows the function q for perturbed values of c, d from (27), revealing that q is still rather similar to a sine curve.

The remaining problem is the non-injectivity of the arcsine function. In fact (14) and (12) give that if we have a particular solution of $p(t)$, the following functions are solutions as well:

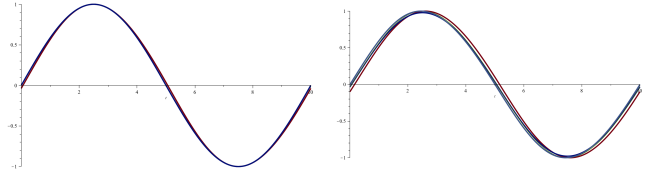$$p(t) + i\,10 \quad \text{and} \quad 5 + i\,10 - 2t - p(t) \qquad (28)$$

Figure 2: *left: visual comparison of the function q fulfilling (27) (red) and the function $\sin\frac{\pi t}{5}$ (blue): the functions are similar but not identical; right: $q(t)$ under perturbations of c, d: dark blue: c = -.20, d = 9.964223389; light blue: c = -.2040811332, d = 9.9; red: c = -.2040811332, d = 10.0; green: q fulfilling (27). All perturbations are similar to the sine function.*
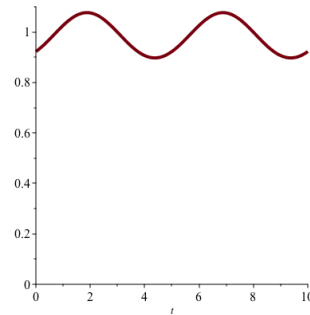

Figure 3: *The function $h(t)$ for the parameter choices (27), (15) is positive for any t.*

for any integer $i \in \mathbb{Z}$. Since we want $p(t)$ as small as possible, we select the solution with the smallest absolute value.

Once (27) is set, we can consider the correctness of (24). Figure 3 shows a plot of $h(t)$ for for the parameters (27), (15). It shows that $p(t) \in [0.8, 1.2]$ for all t, i.e., (24) is safely fulfilled. With this we have finally shown that $\mathbf{g}(t)$ is a hyperbolic trajectory of $\bar{\mathbf{v}}$.

Analysis of p and $\bar{\mathbf{v}}$ After showing that $\mathbf{g}$ is a hyperbolic trajectory of $\bar{\mathbf{v}}$, we still need to show that $\mathbf{v}$ and $\bar{\mathbf{v}}$ are similar, and in particular that $\mathbf{v}$ and $\bar{\mathbf{v}}$ produce LCS of a similar complexity. For this, we analyze the function p describing the time reparametrization of $\bar{\mathbf{v}}$. Figure 4 (left) shows a plot of the time parameters $t + p$ of $\bar{\mathbf{v}}$ over time time period. It can hardly be distinguished from a linear function. Figure 4 (right) shows the function p for $t \in [0, 10]$, indicating that $\|p(t)\| < 0.006\frac{2\pi}{\omega}$ where $\frac{2\pi}{\omega}$ is the the time periodicity of $\mathbf{v}$ and $\bar{\mathbf{v}}$ respectively. We consider p rather small in comparison to the time periodicity. In fact, $|\frac{dp}{dt}|$ is much smaller than 1, which ensures that the time reparametrization in (17) is always regular [Far97]. Also note that $p(t)$ is *not* a sine function, even though it looks similar. This also shows that the DOUBLE GYRE does *not* have a sine curve as hyperbolic trajectory. If it had, $p(t)$ would be constant.

We further compare $\mathbf{v}$ and $\bar{\mathbf{v}}$. Note that for $t = \frac{5}{2}$, $\mathbf{v}$ and $\bar{\mathbf{v}}$ are almost identical because figure 4(right) shows that p is almost zero. The largest difference between $\mathbf{v}$ and $\bar{\mathbf{v}}$ can be expected when $\|p\|$ becomes maximal, e.g., for $t = 0$. Figure 5 shows the LIC images
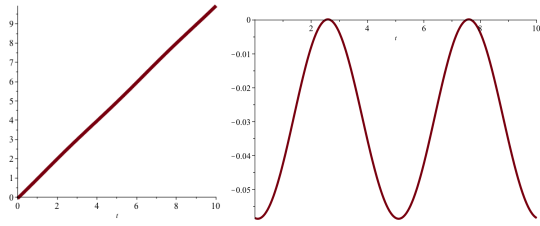
Figure 4: *left: the function $p(t) + t$ is almost linear for $t \in [0,10]$; right: the function $p(t)$ is rather small in comparison to the periodicity time*
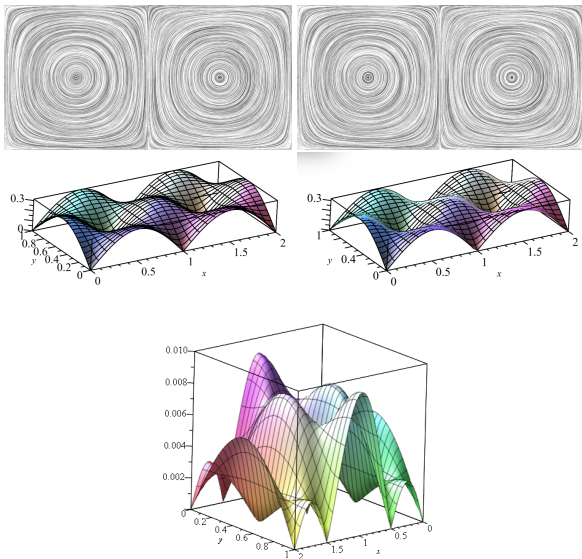

Figure 5: *LIC of $\mathbf{v}$ and $\overline{\mathbf{v}}$ (upper line), height fields of $\|\mathbf{v}\|$ and $\|\overline{\mathbf{v}}\|$ (middle line) for $t = 0$; height field of $\|\mathbf{v} - \overline{\mathbf{v}}\|$ (lower line): $\mathbf{v}$ and $\overline{\mathbf{v}}$ are rather similar.*

of $\mathbf{v}$ and $\overline{\mathbf{v}}$ as well as $\|\mathbf{v}\|$ and $\|\overline{\mathbf{v}}\|$ as height fields for $t = 0$. Figure 5 (lower line) also shows $\|\mathbf{v} - \overline{\mathbf{v}}\|$ being in the range between 0 and 0.01, in comparison to $\|\mathbf{v}\|, \|\overline{\mathbf{v}}\|$ being in the range between 0 and 0.3.

The similarity of $\mathbf{v}$ and $\overline{\mathbf{v}}$ does not necessarily mean that they produce similar LCS because minimal differences in $\mathbf{v}$ and $\overline{\mathbf{v}}$ could be accumulated during the LCS integration. To test this, in figure 6 we compute the FTLE fields for $\mathbf{v}$ and $\overline{\mathbf{v}}$ for different integration times. It shows that $\mathbf{v}$ and $\overline{\mathbf{v}}$ give similar FTLE fields. Furthermore, in figure 7 we give a direct comparison of an FTLE ridge in $\mathbf{v}$ and $\overline{\mathbf{v}}$ for a specific integration time. The position of the ridge differs only in a small amount. This is an indicator that $\overline{\mathbf{v}}$ gives LCS of a similar complexity as the Double Gyre $\mathbf{v}$.

We conclude this section with the recommendation: for further analyses of LCS, it is recommended to replace the DOUBLE GYRE $\mathbf{v}$ by the *Modified Double Gyre* $\overline{\mathbf{v}}$ because with this we lose almost nothing ($\mathbf{v}$ and $\overline{\mathbf{v}}$ are similar and produce similar LCS) but win a lot:

the availability of ground truth hyperbolic trajectories and hence ground truth LCS.

6. Results

The availability of ground truth hyperbolic trajectories allows us to compute ground truth LCS by computing their stable and unstable manifolds. For this we use an approach similar to [MBES16, ÜSE13, SW10]: we integrate a generalized streak surface starting in the neighborhood of $\mathbf{g}(t)$. This way the LCS boundary $\mathbf{l}(t, \tau)$ is obtained by

$$\mathbf{l}(t,\tau) = \overline{\phi}_{t+\tau}^{-\tau}(\mathbf{g}(t+\tau) + \mu \overline{\mathbf{e}}(\mathbf{g}(t+\tau), t+\tau)), \qquad (29)$$

where $\overline{\mathbf{e}}(\mathbf{x},t)$ describes the eigenvector corresponding to the negative eigenvalue of $\nabla \overline{\mathbf{v}}(\mathbf{x},t)$, and μ is a small offset. In order to extract the LCS, we do not actually integrate a meshed streak surface as seen in figure 8. Instead, we integrate single path lines starting at $\mathbf{g}(t_i), t_i \in [t...t + \tau]$ in backward direction just long enough that the end point of a single path line reaches time t. If the distance d of two adjacent end points x_i and x_{i+1} starting at $\mathbf{g}(t_i)$ and $\mathbf{g}(t_{i+1})$, respectively, exceeds a distance threshold d_{min} another path line will be integrated starting at $\mathbf{g}(\frac{1}{2}(t_i + t_{i+1}))$. To obtain a smooth LCS curve this process is repeated until the distance from x_i to its new successor falls below d_{min}. Figure 8 illustrates the construction of the LCS boundaries.

Our ground truth LCS line (29) comes with two parameters τ and μ that need to be analyzed. Figure 9 shows $\mathbf{l}(0,60)$ for different choices of μ. Figure 10 shows $\mathbf{l}(0,\tau)$ for $\mu = 1e{-}10$ for different choices of τ. Figure 11 shows the arc length of $\mathbf{l}(0,\tau)$ for different choices of μ, τ. It shows that arc length of $\mathbf{l}$ shows an exponential growing on both μ and τ. While for μ this behavior can be easily explained (a particle needs an exponential time to move away from a location close to the hyperbolic trajectory), the exponential dependency on τ seems to be a property of the particular data set and not of general LCS. Note that the exponential dependency on τ appears for larger μ, i.e., when $\mathbf{l}$ has a certain length due to multiple foldings.

With the ground truth hyperbolic trajectory we obtain long LCS boundaries under low computation times: In our tests the longest computation time was 58 seconds with $\mu = 0.1$ and $\tau = 60$, which gives an arc length of about $11,000$.

6.1. Evaluation of a FTLE ridge extractor

We apply our ground truth hyperbolic trajectories to evaluate an existing numerical approach to FTLE ridge line extraction especially focusing on rather long integration times. It is known that FTLE ridge lines represent LCS. However, their numerical extraction is challenging: firstly, FTLE fields tend to have extreme gradients, making a careful adaptive subdivision necessary to get a reliable ridge line geometry. Secondly, FTLE can produce false positives, i.e. ridge lines due to high sheer instead of flow separation. We consider the particular approach [WRT18]. We compare the quality of the extracted ridges with the ground truth LCS of $\overline{\mathbf{v}}$. Figure 13a shows the FTLE field of $\overline{\mathbf{v}}$ for $t = 0$ and $\tau = 25$ in a color coding similar to figure 6. Figure 13b shows the extracted FTLE ridge geometry by the approach in [WRT18]. This needs to
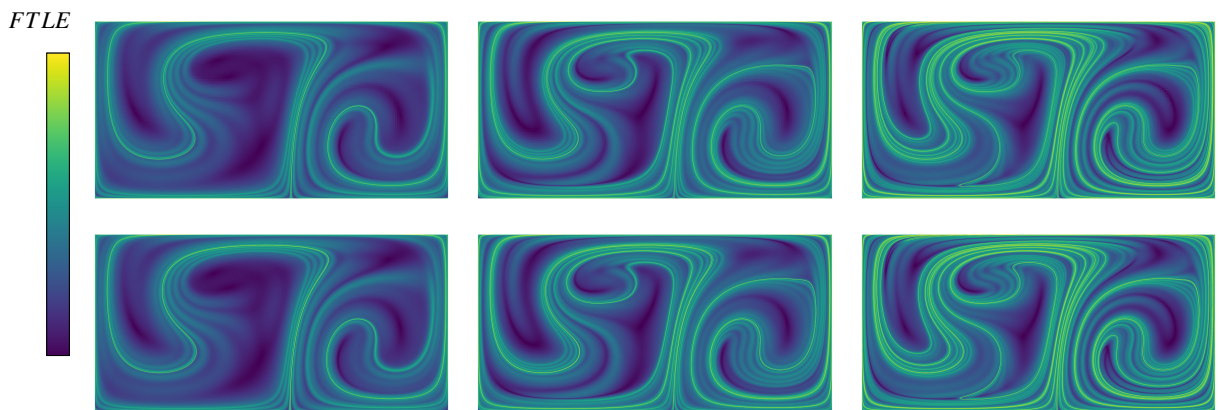
Figure 6: *Comparison of FTLE fields of the* DOUBLE GYRE**v** *(top) and the* Modified Double Gyre $\overline{\mathbf{v}}$ *(bottom) for $t = 0.0$ and $\tau = 10.0$ (left), $\tau = 15.0$ (middle) and $\tau = 25.0$ (right). FTLE of* **v** *and* $\overline{\mathbf{v}}$ *look rather similar, indicating that* $\overline{\mathbf{v}}$ *is obtained from* **v** *by only a minimal modification.*
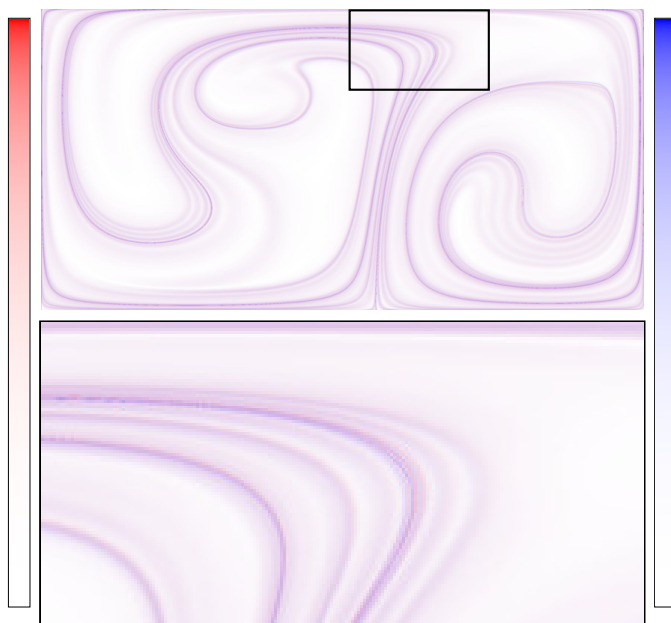

Figure 7: *Combined visualization of the FTLE fields (top) with close up of selected areas (bottom) of the* DoubleGyre Shadden et al. *(red)* **v** *and the* Modified DoubleGyre $\overline{\mathbf{v}}$ *(blue) for $t = 0.0$ and $\tau = 20.0$. Positions of characteristic FTLE ridges of* **v** *and* $\overline{\mathbf{v}}$ *show only small differences, indicating that both vector fields are rather similar.*
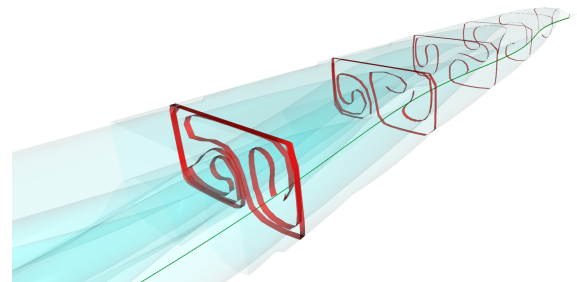

Figure 8: *Ground truth hyperbolic trajectory line as seed curve (green) of a generalized streak surface; time slices (red) of the generalized streak surface correspond to the LCS curve.*

be compared with our new ground truth LCS that is shown in figure 13c. The comparison of figures 13b and 13c show that [WRT18] finds all FTLE ridges but fails to deliver them as connected line structures. Moreover, [WRT18] find a number of false positives, i.e., FTLE ridges that are not LCS.

6.2. Evaluation of a local approach to extract hyperbolic trajectories

With the help of the ground truth hyperbolic trajectory we evaluate the local approach [MBES16] to extract hyperbolic trajectories by relating them to 2D space-time bifurcation lines. It starts with the initial line of vanishing acceleration $\mathbf{a} = \nabla \mathbf{v} \mathbf{v} + \mathbf{v}_t = \mathbf{0}$ or vanishing jerk $\mathbf{b} = \nabla \mathbf{a} \mathbf{v} + \mathbf{a}_t = \mathbf{0}$ respectively as starting values following by an optimization to move the initial lines towards a path line.

Figure 14 (upper) shows the ground truth hyperbolic trajectory of $\overline{\mathbf{v}}$ in space-time together with lines $\mathbf{a} = \mathbf{0}$, $\mathbf{b} = \mathbf{0}$, $\overline{\mathbf{v}} = \mathbf{0}$, and $\mathbf{x} = (1,0)^T$. All of them differ from the ground truth hyperbolic trajectory. While the line $\mathbf{a} = \mathbf{0}$ as suggested in [MBES16] is closest

Figure 9: *Impact of varying μ for fixed τ = 60. Left: μ = 1e−2, arc length = 6 943.47. Center: μ = 1e−4, arc length = 3 407.08. Right: μ = 1e−8, arc length = 837.985.*

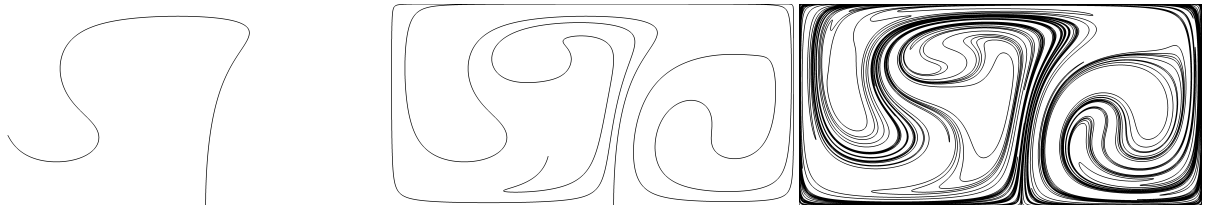**Figure 10:** *Impact of varying τ for fixed μ = 1e−10. Left: τ = 30, arc length = 1502.36. Center: τ = 40, arc length = 837.985. Right: τ = 60, arc length = 418.808.*
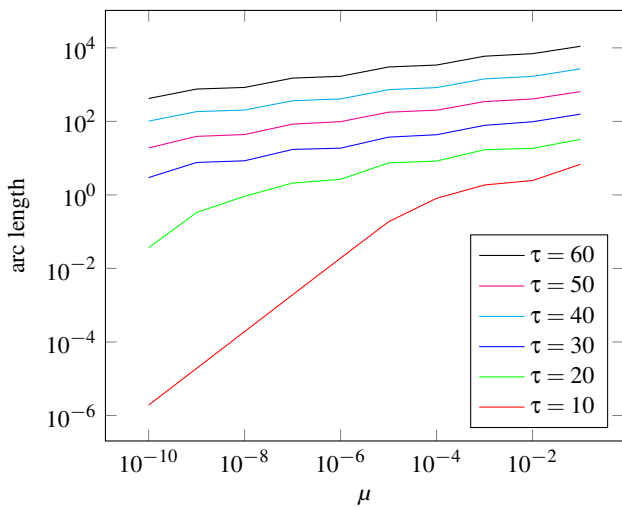

Figure 11: *Arc lengths of LCS curves with varying μ and τ in log-log plot.*

to the ground truth of all candidates, it is not clear if this a general property or it only holds for the particular data set.

In a second experiment, we started the optimization described in [MBES16] from the initial lines $\mathbf{a} = \mathbf{0}$, $\mathbf{b} = \mathbf{0}$, $\bar{\mathbf{v}} = \mathbf{0}$, and $\mathbf{x} = (1,0)^T$. For all the initial curves except $\mathbf{b} = \mathbf{0}$, the optimization converges towards the ground truth hyperbolic trajectory, as shown in figure 14 (lower). Also this experiment does not reveal any special property of the line $\mathbf{a} = \mathbf{0}$.

To further analyze the technique in [MBES16], we analyze if it guarantees to always find a hyperbolic trajectory. For this, we consider a simple new test data set $\mathbf{w}$ that is different to $\bar{\mathbf{v}}$ but is

constructed in the same spirit:

$$\mathbf{w}(\mathbf{x},t) = \frac{81 - (x^2 + y^2)^2}{160} \begin{pmatrix} -x + \cos(t) - 2\sin(t) \\ y - \sin(t) + 2\cos(t) \end{pmatrix} \quad (30)$$

that has a hyperbolic trajectory at $\mathbf{g_w}(t) = (\cos t, \sin t)^T$. (To show that $\mathbf{g_w}$ is indeed a hyperbolic trajectory $\mathbf{w}$, we need to check that $\mathbf{g_w}$ is a path line of $\mathbf{w}$ fulfilling (1), (2), which can be shown by straightforward computations.)

Figure 12 (left) shows the ground truth hyperbolic trajectory $\mathbf{g_w}(t)$ in space-time which passes through the intersections of forward and backward FTLE ridges at times $t_0 = -5$, $t_1 = 0$ and $t_2 = 5$. The center column of figure 12 shows the lines $\mathbf{a} = \mathbf{0}$ (orange) and $\mathbf{b} = \mathbf{0}$ (purple). This is possible by omitting the solutions located at the circle with radius $r = 3$ (gray cylinder in space-time) where $\mathbf{a}$ and $\mathbf{b}$ are also equal to $\mathbf{0}$. The right column of figure 12 shows that the application of [MBES16] to $\mathbf{a} = \mathbf{0}$ and $\mathbf{b} = \mathbf{0}$ does not converge to $\mathbf{g_w}$.

With this, figure 12 is a counterexample that [MBES16] always finds hyperbolic trajectories.

7. Discussion

This is perhaps not a usual CGF paper because it neither describes a new technical contribution nor a classical application, system or evaluation. As such, it does not fit into any standard category of Visualization or Computer Graphics. However, we believe that the introduction of a new benchmark data set with provable properties – closed-form ground truth hyperbolic trajectories – is useful for testing new techniques for extracting LCS and this way brings Flow Visualization forward.

The new data set focuses on forward LCS. A very similar approach can be applied to treat backwards LCS: a slight time-
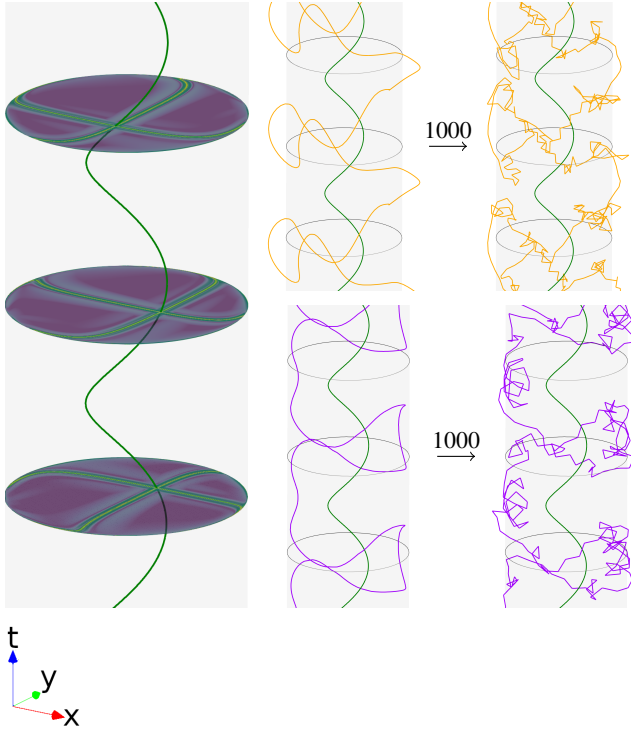
Figure 12: *Left: ground truth hyperbolic trajectory* $\mathbf{g_w}(t) = (\cos t, \sin t)^T$ *of* $\mathbf{w}(\mathbf{x}, t)$ *counterexample in green passing through intersections of forward and backward FTLE ridges at times* $t_0 = -5$, $t_1 = 0$ *and* $t_2 = 5$. *Gray cylinder has radius* $r = 3$. *Center column:* $\mathbf{a} = \mathbf{0}$ *(orange) and* $\mathbf{b} = \mathbf{0}$ *(purple) of counterexample with ground truth hyperbolic trajectory Right column: application of [MBES16] to* $\mathbf{a} = \mathbf{0}$ *and* $\mathbf{b} = \mathbf{0}$ *after 1000 iterations. Both* $\mathbf{a} = \mathbf{0}$ *and* $\mathbf{b} = \mathbf{0}$ *do not converge to the ground truth hyperbolic trajectory.*

reparametrization $\bar{\mathbf{v}}'$ of $\mathbf{v}$ to have the curve

$$\mathbf{g}'(t) = \begin{pmatrix} c' \sin(r'(t)) + 1 \\ 1 \end{pmatrix}$$

as bifurcation line. With this we can even construct a test data set with ground truth hyperbolic trajectories for both forward and backward LCS:

$$\bar{\bar{\mathbf{v}}} = (1 - y)\bar{\mathbf{v}} + y\bar{\mathbf{v}}'$$

However, note that $\bar{\bar{\mathbf{v}}}$ is no longer a time-reparametrization of $\mathbf{v}$ anymore.

While $\bar{\mathbf{v}}$ has a ground truth hyperbolic trajectory, the computation of the LCS boundaries still requires a numerical integration. While this can be considered to be stable – it involves only the flow map and not its gradient – it would be nice to have a non-trivial data set similar to $\mathbf{v}$ where the whole LCS line is given as a ground truth closed form curve. At present, we are not aware of any such solution.
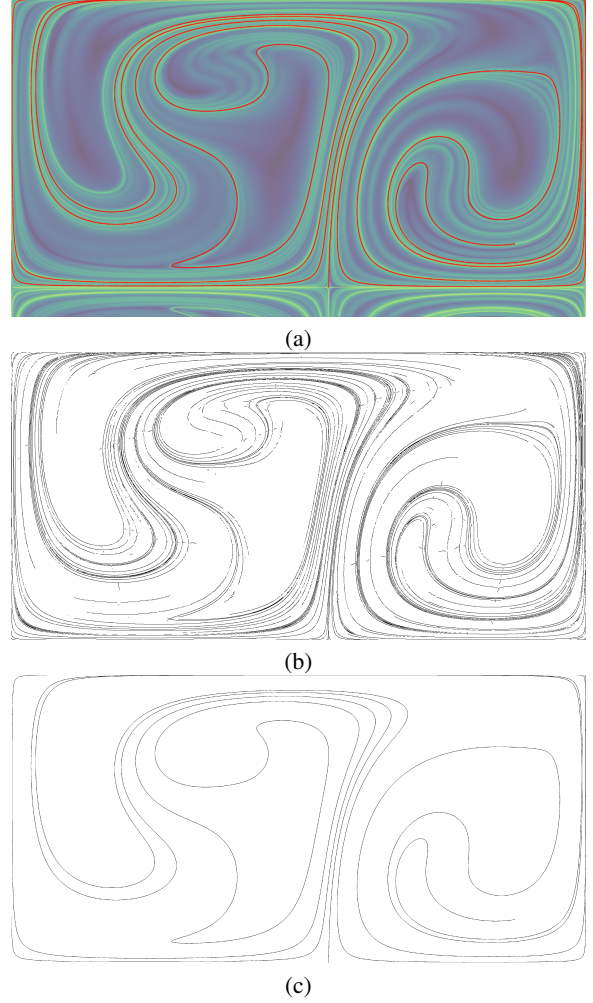
(a)

(b)

(c)

Figure 13: *Comparison between LCS extracted by FTLE ridges and the ground truth. (a) FTLE field for the* Modified Double Gyre *data set with overlay of the ground truth LCS (red) (note: domain was extended to* $[-0.1, 1.0] \times [0.0, 2.0]$ *to better visualize the LCS origin). (b) FTLE ridges extracted by the approach in [WRT18] (c) ground truth LCS*

Appendices

Proof that (19) *and* (20) *are the solutions of* (18)*:*
We rewrite the Double Gyre by Shadden et al. (7)–(11) *by*

$$a = a(t) = \varepsilon \sin(\omega t) \tag{31}$$

$$f = f(x, t) = x + ax(x - 2) \tag{32}$$

$$f_x = \frac{df}{dx} = 1 + 2a(x - 1) \tag{33}$$

$$\psi(\mathbf{x}, t) = A \sin(\pi f) \sin(\pi y) \tag{34}$$

$$\mathbf{v}(\mathbf{x}, t) = \begin{pmatrix} -\psi_y \\ \psi_x \end{pmatrix} = \begin{pmatrix} -A\pi \sin(\pi f) \cos(\pi y) \\ A\pi f_x \cos(\pi f) \sin(\pi y) \end{pmatrix} \tag{35}$$
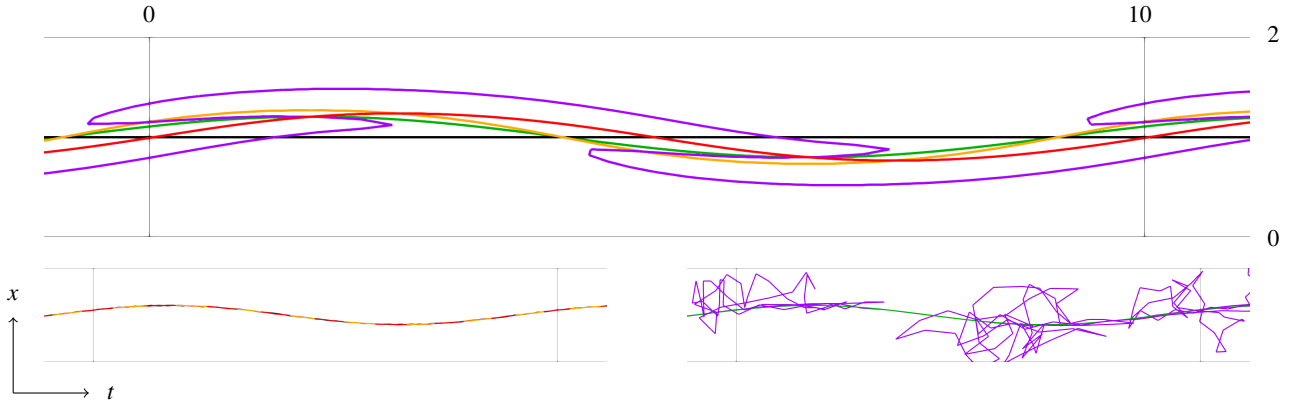
Figure 14: *Lines of $\bar{\mathbf{v}}$. green: ground truth hyperbolic trajectory, red: $\bar{\mathbf{v}} = \mathbf{0}$, orange: $\mathbf{a} = \mathbf{0}$, purple: $\mathbf{b} = \mathbf{0}$, black $\mathbf{x} = (1,0)^T$. All curves lie in the plane $y = 0$. Bottom: $\bar{\mathbf{v}} = \mathbf{0}$, $\mathbf{a} = \mathbf{0}$ and $\mathbf{x} = (1,0)^T$ (left) converge to the groundtruth hyperbolic trajectory. $\mathbf{b} = \mathbf{0}$ does not converge (right).*

which is identical to (7)–(11). Based on this, the *Modified Double Gyre* (17) writes as

$$\bar{a} = \varepsilon \sin(\omega(t+p)) \tag{36}$$

$$\bar{f} = x + \bar{a}x(x-2) \tag{37}$$

$$\bar{f}_x = 1 + 2\bar{a}(x-1) \tag{38}$$

$$\bar{\mathbf{v}}(\mathbf{x},t) = \begin{pmatrix} -A\pi\sin(\pi\bar{f})\cos(\pi y) \\ A\pi\bar{f}_x\cos(\pi\bar{f})\sin(\pi y) \end{pmatrix}. \tag{39}$$

Observing $\bar{\mathbf{v}}$ along the ground truth curve $\mathbf{g}(t) = \begin{pmatrix} g(t) \\ 0 \end{pmatrix}$ as defined in (16), we realize that the second component of $\mathbf{g}$ is always zero, giving the following description of $\bar{\mathbf{v}}(\mathbf{g}(t),t)$:

$$\bar{\bar{f}} = g + \bar{a}g(g-2) \tag{40}$$

$$\bar{\mathbf{v}}(\mathbf{g}(t),t) = \begin{pmatrix} -A\pi\sin(\pi\bar{\bar{f}}) \\ 0 \end{pmatrix}. \tag{41}$$

Since $\frac{d\mathbf{g}(t)}{dt} = \begin{pmatrix} c\omega\cos(r) \\ 0 \end{pmatrix}$, (41) gives that (18) is fulfilled for

$$-A\pi\sin(\pi\bar{\bar{f}}) = A\pi\sin(\pi\bar{\bar{f}} - \pi) = c\omega\cos(r) \tag{42}$$

which is equivalent to

$$\bar{\bar{f}} = \frac{\arcsin\left(\frac{c\omega\cos(r)}{A\pi}\right)}{\pi} + 1. \tag{43}$$

Rewriting (40) and keeping $g = c\sin(r) + 1$ in mind gives

$$\bar{a} = \frac{\bar{\bar{f}} - c\sin(r) - 1}{c^2\sin(r)^2 - 1}. \tag{44}$$

Inserting (43) into (44) gives

$$\bar{a} = \frac{\arcsin\left(\frac{c\omega\cos(r)}{A\pi}\right) - \pi c\sin(r)}{\pi(c^2\sin(r)^2 - 1)} \tag{45}$$

Rewriting (36) gives

$$p = \frac{\arcsin\left(\frac{\bar{a}}{\varepsilon}\right)}{\omega} - t. \tag{46}$$

(45) and (46) prove (19) and (20) for $q = \frac{\bar{a}}{\varepsilon}$.

Proof that the Jacobian matrix (21) along $\mathbf{g}$ has the form (22), (23)

Starting from (39), we compute the Jacobian of the *Modified Double Gyre* as

$$\bar{\mathbf{J}}(\mathbf{x},t) = \nabla\bar{\mathbf{v}}(\mathbf{x},t) = \tag{47}$$

$$\begin{pmatrix} -A\pi^2\bar{f}_x\cos(\pi\bar{f})\cos(\pi y) & A\sin(\pi\bar{f})\pi^2\sin(\pi y) \\ -A\pi\sin(\pi y)\frac{d(\bar{f}_x\cos(\pi\bar{f}))}{dx} & A\pi^2\bar{f}_x\cos(\pi\bar{f})\cos(\pi y) \end{pmatrix}.$$

Observing $\bar{\mathbf{J}}$ along the ground truth curve $\mathbf{g}(t)$, we use again the fact that the second component of $\mathbf{g}(t)$ is zero, resulting in

$$\bar{\mathbf{J}}(t) = \begin{pmatrix} \bar{h} & 0 \\ 0 & -\bar{h} \end{pmatrix} \tag{48}$$

with

$$\bar{\bar{f}}_x = 1 + 2\bar{a}(g-1) \tag{49}$$

$$\bar{h} = -A\pi^2\bar{\bar{f}}_x\cos(\pi\bar{\bar{f}}). \tag{50}$$

With this it remains to show that $\bar{h} = h$ as defined in (23). For this we insert (16), (40), (49) into (50), resulting in

$$\bar{h} = -2A\cos\left(\pi(\bar{a}(\sin(r)^2c^2 - 1) + c\sin(r) + 1)\right)\pi^2\left(\bar{a}c\sin(r) + \frac{1}{2}\right).$$

Then (45) and $q = \frac{\bar{a}}{\varepsilon}$ gives $h = \bar{h}$ for $A > 0$.

References

[ACSZ13] ANDRADE-CANTO F., SHEINBAUM J., ZAVALA SANSÓN L.: A Lagrangian approach to the Loop Current eddy separation. *Nonlinear Processes in Geophysics 20*, 1 (2013), 85–96. 3

[AU01] ADIGA B., UCE B.: Global bifurcation of shilnikov type in a double-gyre ocean model. *Journal of Physical Oceanography 31* (09 2001). 1

[BAC93] BAEK B. J., ARMALY B. F., CHEN T.: Measurements in buoyancy-assisting separated flow behind a vertical backward-facing step. 2

[BK17] BANISCH R., KOLTAI P.: Understanding the geometry of transport: Diffusion maps for lagrangian trajectory data unravel coherent sets. *Chaos: An Interdisciplinary Journal of Nonlinear Science 27*, 3 (Mar 2017), 035804. 1

[BT13] BARAKAT S. S., TRICOCHE X.: Adaptive Refinement of the Flow Map Using Sparse Samples. *IEEE Trans. Vis. Comput. Graph. 19*, 12 (2013), 2753–2762. 3

[CLP*07] COULLIETTE C., LEKIEN* F., PADUAN J. D., HALLER G., MARSDEN J. E.: Optimal Pollution Mitigation in Monterey Bay Based on Coastal Radar Data and Nonlinear Dynamics. 3

[Cra03] CRAWFIS R.: Tornado data set generator, 2003. 2

[Far97] FARIN G.: *Curves and Surfaces for Computer Aided Geometric Design*, 4th ed. Academic Press, Boston, 1997. 5

[FH13] FARAZMAND M., HALLER G.: Attracting and repelling lagrangian coherent structures from a single computation. *Chaos: An Interdisciplinary Journal of Nonlinear Science 23*, 2 (2013), 023101. 2

[FP09] FROYLAND G., PADBERG K.: Almost-invariant sets and invariant manifolds — connecting probabilistic and geometric descriptions of coherent structures in flows. *Physica D: Nonlinear Phenomena 238*, 16 (2009), 1507 – 1523. 3

[FS16] FROYLAND G., SANTITISSADEEKORN N.: Optimal mixing enhancement, 2016. 3

[GGT17] GÜNTHER T., GROSS M., THEISEL H.: Generic objective vortices for flow visualization. *ACM Transactions on Graphics (Proc. SIGGRAPH) 36*, 4 (2017), 141:1–141:11. 2

[GGTH07] GARTH C., GERHARDT F., TRICOCHE X., HANS H.: Efficient Computation and Visualization of Coherent Structures in Fluid Flow Applications. *IEEE Transactions on Visualization and Computer Graphics 13*, 6 (2007), 1464–1471. 3

[GKT16] GÜNTHER T., KUHN A., THEISEL H.: MCFTLE: Monte Carlo Rendering of Finite-Time Lyapunov Exponent Fields. *Computer Graphics Forum (Proc. EuroVis) 35*, 3 (2016), 381–390. 3

[GLT*09] GARTH C., LI G.-S., TRICOCHE X., HANSEN C. D., HAGEN H.: Visualization of Coherent Structures in Transient 2D Flows. Springer, Berlin, Heidelberg, 2009, pp. 1–13. 3

[GOPT11] GERMER T., OTTO M., PEIKERT R., THEISEL H.: Lagrangian Coherent Structures with Guaranteed Material Separation. *Computer Graphics Forum (Proc. EuroVis) 30*, 3 (2011), 761–770. 3

[GSM*14] GÜNTHER T., SCHULZE M., MARTINEZ ESTURO J., RÖSSL C., THEISEL H.: Opacity optimization for surfaces. *Computer Graphics Forum (Proc. EuroVis) 33*, 3 (2014), 11–20. 2

[Hal00] HALLER G.: Finding finite-time invariant manifolds in two-dimensional velocity fields. *Chaos (Woodbury, N.Y.) 10* (04 2000), 99–108. 1, 2

[Hal01] HALLER G.: Distinguished material surfaces and coherent structures in three-dimensional fluid flows. *Physica D: Nonlinear Phenomena 149*, 4 (2001), 248–277. 3

[Hal02a] HALLER G.: Lagrangian coherent structures from approximate velocity data. *Physics of Fluids 14*, 6 (2002), 1851–1861. 2

[Hal02b] HALLER G.: Lagrangian coherent structures from approximate velocity data. *Physics of Fluids 14*, 6 (2002), 1851–1861. 3

[Hal11] HALLER G.: A variational theory of hyperbolic lagrangian coherent structures. *Physica D: Nonlinear Phenomena 240*, 7 (2011), 574 – 598. 2

[Hal15] HALLER G.: Lagrangian Coherent Structures. *Annual Review of Fluid Mechanics 47* (2015), 137–62. 2, 3

[HBJG16] HUMMEL M., BUJACK R., JOY K. I., GARTH C.: Error estimates for Lagrangian flow field representations. *Proceedings of the Eurographics / IEEE VGTC Conference on Visualization: Short Papers* (2016), 7–11. 3

[HFB*17] HADJIGHASEM A., FARAZMAND M., BLAZEVSKI D., FROYLAND G., HALLER G.: A critical comparison of lagrangian methods for coherent structure detection. *Chaos: An Interdisciplinary Journal of Nonlinear Science 27*, 5 (May 2017), 053104. 2

[HP98] HALLER G., POJE A.: Finite time transport in aperiodic flows. *Physica D: Nonlinear Phenomena 119*, 3 (1998), 352 – 380. 3

[HS11] HALLER G., SAPSIS T.: Lagrangian coherent structures and the smallest finite-time Lyapunov exponent. *Chaos 21*, 2 (June 2011), 023115. 2

[HS19a] HARRISON D. E., STALOS S.: On the wind-driven ocean circulation. 1

[HS19b] HOFMANN L., SADLO F.: The Dependent Vectors Operator. *Computer Graphics Forum 38*, 3 (2019). 3

[HSW11] HLAWATSCH M., SADLO F., WEISKOPF D.: Hierarchical Line Integration. *IEEE Transactions on Visualization and Computer Graphics 17*, 8 (2011), 1148–1163. 3

[HY00] HALLER G., YUAN G.: Lagrangian coherent structures and mixing in two-dimensional turbulence. *Physica D: Nonlinear Phenomena 147*, 3-4 (2000), 352–370. 3

[KC93] KUMAR R., CONOVER T.: Flow visualization studies of a swirling flow in a cylinder. *Experimental thermal and fluid science 7*, 3 (1993), 254–262. 2

[KRWT12] KUHN A., ROSSL C., WEINKAUF T., THEISEL H.: A benchmark for evaluating FTLE computations. *IEEE Pacific Visualization Symposium 2012, PacificVis 2012 - Proceedings* (2012), 121–128. 3

[LCM*05] LEKIEN F., COULLIETTE C., MARIANO A. J., RYAN E. H., SHAY L. K., HALLER G., MARSDEN J.: Pollution release tied to invariant manifolds: A case study for the coast of Florida. *Physica D: Nonlinear Phenomena* (2005). 3

[LSM06] LEKIEN F., SHADDEN S., MARSDEN J.: Lagrangian coherent structures in n-dimensional systems. *Journal of Mathematical Physics 48* (2006), 065404. 2

[MBES16] MACHADO G. M., BOBLEST S., ERTL T., SADLO F.: Space-time bifurcation lines for extraction of 2D Lagrangian coherent structures. *Computer Graphics Forum 35*, 3 (2016), 91–100. 3, 6, 7, 8, 9

[Mof88] MOFFATT H. K.: An informal introduction to theoretical fluid mechanics. by james lighthill. clarendon press, 1986. 260 pp. *Journal of Fluid Mechanics 195* (1988). 2

[MSE13] MACHADO G. M., SADLO F., ERTL T.: Local Extraction of Bifurcation Lines. 3

[MSWI03] MANCHO A., SMALL D., WIGGINS S., IDE K.: Computation of stable and unstable manifolds of hyperbolic trajectories in two-dimensional, aperiodically time-dependent vector fields. *Physica D: Nonlinear Phenomena 182 (3-4)* (8 2003), 188 – 222. Publisher: Elsevier Science BV Other identifier: IDS number 713LT. 3

[OHH15] ONU K., HUHN F., HALLER G.: Lcs tool: A computational platform for lagrangian coherent structures. *Journal of Computational Science 7* (2015), 26 – 36. 2

[PC87] PERRY A. E., CHONG M. S.: A Description of Eddying Motions and Flow Patterns Using Critical-Point Concepts. *Annual Review of Fluid Mechanics 19*, 1 (1987), 125–155. 3

[PNNS86] PAYNE F., NG T., NELSON R., SCHIFF L.: Visualization and flow surveys of the leading edge vortex structure on delta wing planforms. In *24th Aerospace Sciences Meeting* (1986), p. 330. 2

[PNNS88] PAYNE F., NG T., NELSON R., SCHIFF L.: Visualization and wake surveys of vortical flow over a delta wing. *AIAA journal 26*, 2 (1988), 137–143. 2

[PPF*11] POBITZER A., PEIKERT R., FUCHS R., THEISEL H., HAUSER H.: Filtering of FTLE for Visualizing Spatial Separation in Unsteady 3D Flow. In *Proc. TopoInVis* (2011). 3

[RG19] ROJO I. B., GÜNTHER T.: Vector field topology of time-dependent flows in a steady reference frame. *IEEE Transactions on Visualization and Computer Graphics (Proc. IEEE Scientific Visualization)* (2019). 3

[RK94] ROM-KEDAR V.: Homoclinic tangles-classification and applications. *Nonlinearity 7*, 2 (mar 1994), 441–473. 3

[RSPB11] RYPINA I. I., SCOTT S. E., PRATT L. J., BROWN M. G.: Investigating the connection between complexity of isolated trajectories and lagrangian coherent structures. *Nonlinear Processes in Geophysics 18*, 6 (2011), 977–987. 2

[SFB*12] SCHINDLER B., FUCHS R., BARP S., WASER J., POBITZER A., MATKOVIĆ K., PEIKERT R.: Lagrangian Coherent Structures for Design Analysis of Revolving Doors. *IEEE Transactions on Visualization and Computer Graphics 18*, 12 (2012), 2159–2168. 3

[Sha05] SHADDEN S. C.: Lagrangian Coherent Structures Analysis of time-dependent systems using finite-time Lyapunov exponents. https://shaddenlab.berkeley.edu/uploads/LCS-tutorial/examples.html, 2005. 2

[SLM05] SHADDEN S. C., LEKIEN F., MARSDEN J. E.: Definition and properties of Lagrangian coherent structures from finite-time Lyapunov exponents in two-dimensional aperiodic flows. *Physica D 212*, 7 (2005). 1, 2, 3, 4

[SMW99] SHEN J., MEDJO T. T., WANG S.-C.: On a wind-driven , double-gyre , quasi-geostrophic ocean model : Numerical simulations and structural analysis 1. 1

[SP07] SADLO F., PEIKERT R.: Efficient visualization of Lagrangian coherent structures by filtered AMR ridge extraction. *IEEE Transactions on Visualization and Computer Graphics 13*, 6 (2007), 1456–1463. 3

[SP09] SADLO F., PEIKERT R.: Visualizing Lagrangian Coherent Structures and Comparison to Vector Field Topology. Springer, Berlin, Heidelberg, 2009, pp. 15–29. 3

[SPFT12] SCHINDLER B., PEIKERT R., FUCHS R., THEISEL H.: Ridge Concepts for the Visualization of Lagrangian Coherent Structures. In *Topological Methods in Data Analysis and Visualization II*, Peikert R., Hauser H., Carr H., Fuchs R., (Eds.), Mathematics and Visualization. Springer, 2012, pp. 221–235. 3

[SRP11] SADLO F., RIGAZZI A., PEIKERT R.: Time-Dependent Visualization of Lagrangian Coherent Structures by Grid Advection. In *Topological Methods in Data Analysis and Visualization*. Springer, Berlin, Heidelberg, 2011, pp. 151–165. 3

[STW*06] SHI K., THEISEL H., WEINKAUF T., HAUSER H., HEGE H.-C., SEIDEL H.-P.: Path line oriented topology for periodic 2d time-dependent vector fields. In *Proc. EuroVis 2006* (2006), pp. 139–146. 3

[SW10] SADLO F., WEISKOPF D.: Time-Dependent 2-D Vector Field Topology: An Approach Inspired by Lagrangian Coherent Structures. *Computer Graphics Forum 29*, 1 (2010), 88–100. 3, 6

[ÜSE13] ÜFFINGER M., SADLO F., ERTL T.: A Time-Dependent Vector Field Topology Based on Streak Surfaces. *IEEE Transactions on Visualization and Computer Graphics 19*, 3 (2013), 379–392. 3, 6

[Wig92] WIGGINS S.: Chaotic transport in dynamic systems. *Springer-verlag 92* (01 1992), 28228. 3

[WRT18] WILDE T., RÖSSL C., THEISEL H.: FTLE Ridge Lines for Long Integration Times. *Proceedings IEEE Scientific Visualization Short Papers 2018* (2018). 3, 6, 7, 9

[WRT19] WILDE T., RÖSSL C., THEISEL H.: Recirculation surfaces for flow visualization. *IEEE Transactions on Visualization and Computer Graphics (Proc. IEEE Scientific Visualization 2018) 25*, 1 (2019), 946–955. 3

[YKY91] YOU Z., KOSTELICH E. J., YORKE J. A.: Calculating stable and unstable manifolds. *International Journal of Bifurcation and Chaos 01*, 03 (1991), 605–623. 3